This article is published, please cite :

J.-Y. Raty, M. Schumacher, P. Golub, V. L. Deringer, C. Gatti, M. Wuttig, *Adv. Mater.* 2018, 1806280.
https://doi.org/10.1002/adma.201806280

A quantum-mechanical map for bonding and properties in materials

Jean-Yves Raty[1,2], Mathias Schumacher[3], Pavlo Golub[4], Volker L. Deringer[5], Carlo Gatti[6,7], and Matthias Wuttig[8,9]

[1] CESAM & Physics of Solids, Interfaces and Nanostructures, B5, Université de Liège, B-4000 Sart-Tilman, Belgium

[2] UGA, CEA-LETI, Minatec Campus, 17 rue des Martyrs, Grenoble, 38054, France

[3] Institute for Theoretical Solid State Physics, RWTH Aachen University, 52056 Aachen, Germany

[4] National University of Singapore, Department of Mechanical Engineering, 9 Engineering Drive 1, Singapore 117575, Singapore

[5] Department of Engineering, University of Cambridge, Cambridge CB2 1PZ, United Kingdom

[6] CNR-ISTM, Istituto di Scienze e Tecnologie Molecolari, c/o Dipartimento di Chimica, Università degli Studi di Milano, via Golgi 19, Milano, 20134, Italy

[7] Istituto Lombardo Accademia di Scienze e Lettere, via Brera 28, Milano, 20121, Italy

[8] Institute of Physics IA, RWTH Aachen University, 52056 Aachen, Germany

[9] Peter Grünberg Institute (PGI 10), Forschungszentrum Jülich, 52428 Jülich, Germany

Materials with rationally controlled properties play important parts in the development of new and advanced technologies. Thermoelectrics, which convert waste heat into electricity, rely on the interplay on thermal and electric conductivity[1]; phase-change materials (PCMs) for emerging neuromorphic[2] or photonic[3] applications exhibit an electrical and optical property contrast between amorphous and crystalline phases. All these properties can be traced back, to a significant extent, to the nature of interatomic bonding in materials. However, the physics and materials-science communities have largely approached this question in a phenomenological way. Here we show how this paradigm can be overcome by developing a two-dimensional map based on a quantum-topological description of electron sharing and electron transfer. This map intuitively identifies the fundamental nature of ionic, metallic, and covalent bonding in a range of elements and binary materials. Furthermore, it highlights a distinct region for a mechanism recently termed "metavalent" bonding. Extending this map into the third dimension by including physical properties of application interest, we provide evidence that metavalent bonding cannot be described by any combination of

the three "textbook" mechanisms—it therefore constitutes a fourth fundamental bonding mechanism by accepted definitions. Our work opens up a conceptually new avenue for designing materials: by searching for desired properties in a 3D space and then mapping this back onto the 2D plane of bonding, allowing scientists to navigate structural and composition spaces and to identify promising target materials.

Phenomenological descriptions of bonding in solids have been useful for centuries. Even to the non-scientist, the term "metal" implies reflective, ductile, electrically conducting solids; a "semiconductor" has a narrow band gap across which electrons can be excited by light; all this is based on measurable, macroscopic properties. A portfolio of physical properties—exceptionally large optical and bond polarizability, lattice anharmonicity, and a hitherto unseen bond-breaking mechanism—was recently used to define a concept termed "metavalent" bonding (MVB)[4,5]. Metavalent solids are between the covalent and metallic regimes, but distinctly different from both[4]. This led to a revision of the "resonant bonding" model previously used to describe the bonding in PCMs[6–8], by showing that the response properties of PCMs are fundamentally different from those of resonantly bonded benzene and graphite [4].

To make the next, necessary step beyond such phenomenological models, one needs to understand the quantum-mechanical origins of bonding. Computational methods are widely used to (approximatively) solve Schrödinger's equation and describe the electronic wavefunction with increasingly high confidence, both in gas-phase molecules and in extended systems[9]. Once this wavefunction is known, it allows to determine spatial distribution, localization, kinetic energy, and other properties of the electron—thereby providing numerical tools to quantify the bonding[10–14]. Relationships of such descriptors with the empirical but powerful concepts of (operative) chemistry have been discussed and successfully exploited[15–17].

In this Letter, we now combine the property-based and the quantum-mechanically based perspective to derive a holistic view of bonding in solids, and then show how this directly leads to novel design rules for materials with interesting properties. We analyse a range of elements and compounds: first, with a standard density-functional theory (DFT) approach to bring the Kohn–Sham wavefunctions to self-consistency; then, with a Hartree–Fock (HF) like expression to compute the electron pair density, which describes the correlated motion of electrons (Methods section). The electronic density in the simulation cell is partitioned into so-called

domains or basins Ω_i around the individual nuclei in the Domain Overlap Matrix (DOM) method. DOM analyses have been routinely done for gas-phase molecules, but only very recently extended to the realm of plane-wave DFT and periodic systems[18,19]. We note at the outset that DFT tends to over-delocalise electrons, whereas HF behaves in the opposite way, but this does not qualitatively affect our conclusions.

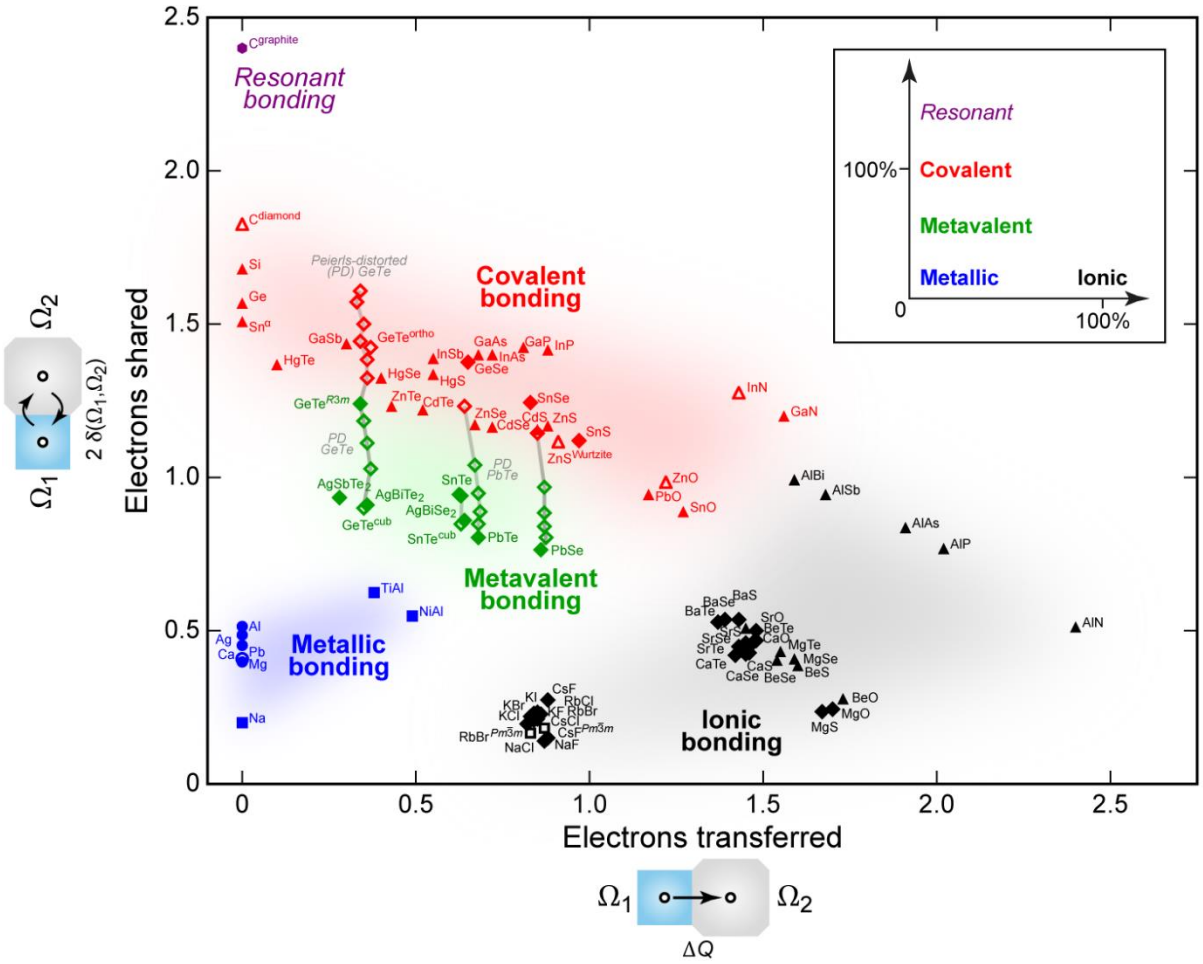

Fig. 1 | A two-dimensional map of electronic interactions and bonding in materials. The amount of electrons transferred (*x*-axis) and shared between neighbouring basins (*y*-axis) are computed using quantum-topological methods; they serve as quantitative measures for the ionic and covalent character, respectively. We here consider elemental and binary phases of main-group elements, adding examples of transition metals, intermetallics, and ternary phases (Table S1); however, the concept is applicable to any solid that can be treated with our computational tools. Symbols indicate structure types: "sp^3"- (tetrahedrally) bonded solids are shown as triangles, distorted and ideal rocksalt-type (octahedrally coordinated) structures as diamonds, body-centred ones as squares; close-packed metal structures as circles. *Filled symbols* denote thermodynamically stable phases (at zero temperature); *open symbols* denote metastable phases. For GeTe, SnTe, PbTe, and PbSe, additional structural intermediates have been generated along the Peierls distortion (PD) coordinate (grey lines as guides to the eye). The sketch in the inset summarises the qualitative conclusions drawn from this map: we consider $2\delta(\Omega_1,\Omega_2) = 2$ to correspond to the sharing of a full electron pair, and therefore

label this as “100%”. Resonantly bonded graphite sheets exhibit more than this one electron pair shared between the atoms; metavalent materials have distinctly less.

The DOM analysis yields a pair of simple descriptors which make it possible to classify or fingerprint any given solid-state material. First, we compute the net charge of an atom, Q_i, by integrating over its basin Ω_i and comparing to the free reference atom: this allows us to assess electron transfer, which is expected to be large in ionic solids (idealised example: Na^+ and Cl^- in table salt) but small otherwise. Second, we compute the delocalisation index for a pair of atoms, $\delta(\Omega_i,\Omega_j)$, which yields the number of electron pairs exchanged or shared between them. Thus, $\delta(\Omega_i,\Omega_j)$ provides a physical measure of a property that classical models associate with covalency, and it is amenable to comparison with formal bond orders. A full pair of electrons shared between neighbouring atoms corresponds to the Lewis picture of a single covalent bond. (Our *y*-axis is defined such that it gives the number of *electrons*; note that some authors prefer to directly report $\delta(\Omega_i,\Omega_j)$ and thus the number of *electron pairs*.)

We now use these descriptors as coordinates to draw a two-dimensional materials map, which is shown in **Fig. 1**. To appreciate its explanatory power, we first discuss archetypes of textbook bonding mechanisms and their location in this map. At the bottom and to the right, NaCl and MgO are generic examples of ionic bonding; the computed degree of electron transfer (0.87 and 1.71 *e*, respectively) approaches the formal picture of Na^+ and Mg^{2+} ions. Looking at covalent solids, we find 1.83 electrons shared for diamond, approximating the Lewis electron-pair bond picture. In all cases, these limits are not reached completely: there is a very small covalent contribution even in NaCl, and there is some valence electron localised on each atom in diamond (albeit no transfer, due to symmetry). The latter aspect becomes more obvious when moving down the fourth main group: diamond-type Si, Ge, and Sn show gradually less electron sharing, concomitant with their increasingly metallic nature. Binary compounds do exhibit electron transfer, but its extent is small in covalent systems and intermetallics, say TiAl. Clear chemical relationships can be observed in the map: e.g., the homologous III–V semiconductors, AlN, AlP, and AlAs, are close to one another; the largest change occurs between the first and second long period (going from AlN to AlP), due to the different size of the valence p-orbital in N and P, as discussed by Burdett[20]. The map also recovers the conventional wisdom that the transition between covalent and ionic bonding is gradual: this is best seen for the isovalent III–V compounds such as GaN and AlSb, where ≈ 1.5 *e* (roughly half of the “cation” valence electrons) are transferred, concomitant with gradually decreasing covalency

(*y*-axis). Finally, we can locate textbook examples of metallic bonding in the map: for example, Na shares only 0.2 *e* (that is, it shows very little yet nonzero covalency), as is characteristic for bonding via delocalised electrons[15]. In short, the map in Fig. 1 identifies the archetypes of ionic, covalent, and metallic bonding in distinctly different and physically meaningful regions.

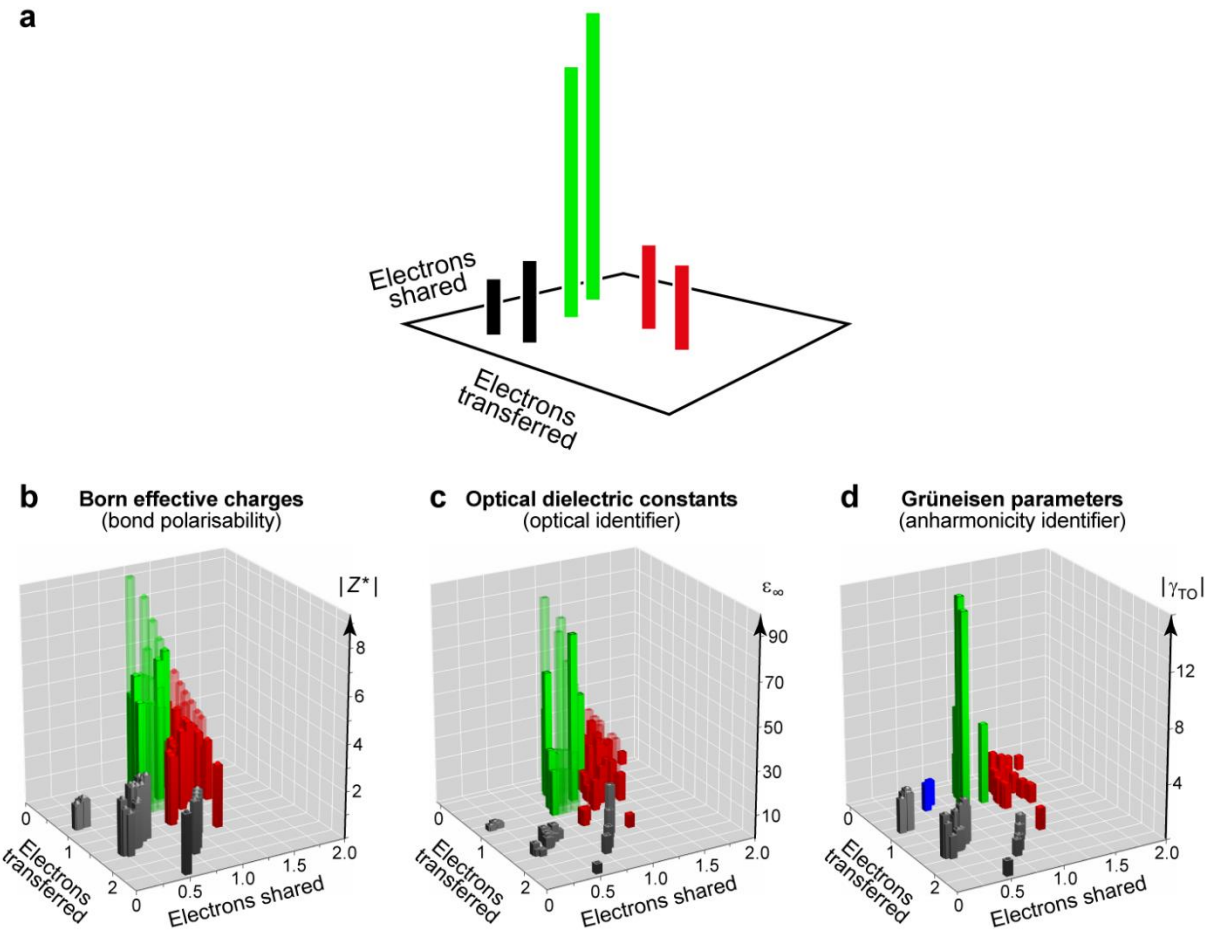

Fig. 2 | Three-dimensional maps defining design rules for materials with desired properties. The base plane is defined as in the 2D map (Fig. 1) and quantifies electrons transferred and shared, respectively. Extending this map in the third dimension (as sketched in panel **a** , we quantify (**b**) Born effective charges, Z^*, (**c**) dielectric constants, ε_∞, and (**d**) absolute transverse optical (TO) mode Grüneisen parameters, $|\gamma_{TO}|$, for binary compounds. Ionic materials in black, covalent in red, metavalent in green (with structural intermediates as semi-transparent bars; see Methods section for details). Metavalent bonding is characterised by unusually high values of all three indicators (green bars), and the 3D plots presented here allow to identify these trends across all of composition space. To design thermoelectrics, for example, one will navigate the base plane to regions of large lattice anharmonicity (panel **c**).

Previous "materials maps" date back to the iconic van Arkel triangle,[21–23] which is widely found in textbooks, and to empirical structure maps for semiconductors based on tabulated

orbital radii[24,25]. We note in passing a recently introduced 2D map that analyses bonding in molecular systems[28]. Perhaps the most closely related to the present work is an electronic-density based study by Mori-Sánchez *et al.*, using "density flatness" (a measure for metallicity), charge transfer (ionicity, similar to the present *x*-axis), and the molecular character as descriptors for the fundamental bonding mechanisms[29]. The use of a "map" has been suggested in 2008 to identify candidate PCMs[26], but has been severely limited to a qualitative (and dichotomic "PCM" / "no PCM") classification of materials, and again based on tabulated orbital radii from which heuristic proxies are constructed for "hybridisation" and ionicity[26]. This concept was later extended using DFT-based descriptors, which are sensitive to atomic structure[27]. However, in all these studies, a crucial aspect has been missing: namely, a rigorous link to physical properties that would enable not only to classify bonding in materials, but to exploit the quantitative bonding information for materials design.

To create this link, let us look more closely at the central region of the map in Fig. 1—which lies in between the three archetypical mechanisms, without clearly belonging to one of them, and is populated by materials as well (green symbols in Fig. 1). One obvious explanation would be that the bonding nature in these materials is a superposition of existing archetypes. For example, hydrogen bonding may have van der Waals, ionic, and covalent contributions, strongly dependent on the distance and nature of the acceptor atom[30]; still, the associated physical properties (e.g., the O–H stretch frequency) change gradually and continuously between the respective limits. In sharp contrast, the MVB materials studied here show a rapid change and anomalously large values for three independent properties. To visualise and analyse this, we now extend the concept of our map into a third dimension, thereby including in the picture numerical values not just for bonding but also for properties (**Fig. 2**). This plot clearly reveals that such simultaneously and anomalously large properties are not found anywhere else within the space of our 2D map. Combining previous phenomenological, property-based evidence[4,5] and the present quantum-topological study, it seems to emerge that MVB is a fourth bonding mechanism beyond the "big three" (ionic, covalent and metallic).

Interest in MVB materials stems from their diverse technological applications, which are directly enabled by properties[31,32]. Beyond its fundamental nature, Fig. 2 therefore suggests a blueprint to tailor properties. For example, it was suggested that bonding in chalcogenides is closely interwoven with a lattice instability, leading to large Grüneisen parameters[33]. Our 3D plot (Fig. 2d) now shows that this anomaly is uniquely linked to MVB—more specifically, to

the border between MVB and metallic bonding. This provides a recipe to identify candidate thermoelectrics[34]: move to MVB materials that border on metals, at around ≈ 0.8 electrons shared. While our map currently contains elements and binary compounds, its extension to ternaries is anticipated to reveal more candidate materials, given that a way can be found to localise the various contacts between different species within the 2D map. To illustrate this, we included in Fig. 1–2 selected ternaries such as $AgSbTe_2$ (Table S1), where we obtained the 2D coordinates by numerically averaging over values for Ag–Te and Sb–Te bonds.

All three *z*-axis quantities in Fig. 2b–d are so-called *response properties*: they do not relate to conventional bond characteristics (such as the localization and delocalization of electrons), but rather to the unconventional way in which the bonds respond to external stimuli. In this light, it is interesting to mention recent studies on the electron organization of many-electron systems in the context of linear response theory[35]. They highlight the profound connection between variances in local electronic position and the momentum operators and the optical conductivity tensor—that is, between electron (de)localization in real and momentum space on the one hand, and the experimentally observable spectroscopic and conductivity properties on the other hand. Our study emphasises the dramatic role such connections may play in a peculiar case of bonding, namely, MVB.

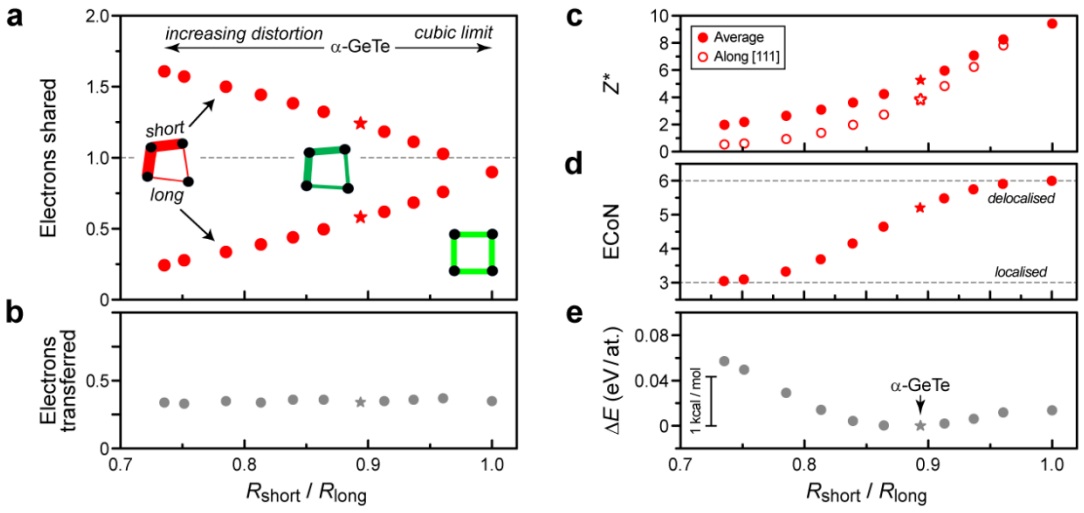

Fig. 3 | Mechanism of the Peierls distortion in materials as described by quantum-based indicators. We analyse a series of GeTe structures, gradually distorted along [111]. We quantify the degree of Peierls distortion (which is largest on the left-hand side) through the ratio of shorter and longer interatomic distances; both become equal in the limit of the ideal, un-

distorted rocksalt type ("cubic limit"). *Left:* (**a**, **b**) the number of electrons shared and transferred (corresponding to the *y*- and *x*-coordinates in Fig. 1, respectively). The Peierls distortion does not affect the amount of electrons transferred (*i.e.*, the ionicity; panel **b**), but it does affect the distribution of electrons shared (panel **a**). Sketches indicate the evolution of electron sharing and structural variation with the gradual variation of the Peierls distortion. *Right:* from top to bottom, we present different bonding indicators and how they are affected by the Peierls distortion: (**c**) the Born effective charges, providing a measurable indicator for the onset of MVB, given as average (filled symbols) and projected on the [111] direction where the effect of distortion is most relevant (open symbols); (**d**) the effective coordination number (ECoN), quantifying the gradual departure from the 8–*N* rule; (e) the energy cost associated with the distortion, relative to α -GeTe, which is very small overall.

The bonding descriptors used here shed new light on a long-standing issue in the structural study of chalcogenide materials. Many MVB materials crystallise in the rocksalt type but some, prominently GeTe, show a small distortion that gives rise to three moderately shorter and three moderately longer bonds. This is referred to as a Peierls distortion. We analyse several structures with gradually varied degree of distortion, including stable α-GeTe and its undistorted cubic form. This allows us to mechanistically understand the transition between covalent (left-hand side) and metavalent (right-hand side) regimes. The progressive Peierls distortion induces a re-distribution of electrons between short Ge–Te and long Ge—Te bonds, which become stronger and weaker, respectively (Fig. 3a). However, the *total* amount of electrons shared is almost invariant; in other words, the total number of electrons forming bonds in crystalline GeTe is unaffected by the Peierls distortion. In the ideal cubic phase, ≈ 1 electron is shared between each of the six neighbours (which is half an electron pair, thus half the covalent limit, and typical of MVB; Fig. 1). Still, even in the most strongly distorted structures (at low R_{short} / R_{long}) there remains non-negligible sharing in the longer bonds. This suggests the absence of any bond/no bond dichotomy: shorter and longer Ge–Te interactions are both associated with "true" bonds and are parts of the same body, with only the repartitioning of electron pairs varying. The number of electrons transferred (Fig. 3b) is unaffected by the Peierls distortion and small overall, dismissing the possibility for substantial ionic contributions to the bonding in this case. Turning to properties once more, the Peierls distortion is concomitant with an electronic instability of which the chemical bond polarisability is indicative (Fig. 3c). The competition between localisation and delocalisation is reflected in a gradually changing, non-integer ECoN (Fig. 3d), and hence the Peierls distortion appears to be decisive in

achieving this delicate balance, especially as its energetic cost is very small (Fig. 3e). Accordingly, small Peierls distortions are frequently encountered in MVB systems.

The data in Figure 3 suggest a route towards property design if one achieves control over the Peierls distortion. This could be done by strain, alloying, creating defects, or nanostructuring (moving along the horizontal axis in Fig. 3, and modifying the ECoN as plotted in Fig. 3d), and this directly allows to tune the properties—increasing thermoelectric efficiency, for example. It also explains how the amorphous phases of PCMs, in which the Peierls distortion becomes extremely large and directionally blurred[36], lose these anomalous properties, creating the electronic and optical property contrast that is exploited in device applications.

References and notes

1. Snyder, G. J. & Toberer, E. S. Complex Thermoelectric Materials. *Nat. Mater.* **7,** 105–114 (2008).

2. Wright, C. D., Liu, Y., Kohary, K. I., Aziz, M. M. & Hicken, R. J. Arithmetic and Biologically-Inspired Computing Using Phase-Change Materials. *Adv. Mater.* **23,** 3408–3413 (2011).

3. Wuttig, M., Bhaskaran, H. & Taubner, T. Phase-change materials for non-volatile photonic applications. *Nat. Photonics* **11,** 465–476 (2017).

4. Wuttig, M., Deringer, V. L., Gonze, X., Bichara, C. & Raty, J.-Y. Incipient Metals: Functional Materials with a Unique Bonding Mechanism, submitted; preprint available at *arXiv:*1712.03588 (2018).

5. Zhu, M. *et al.* Unique Bond Breaking in Crystalline Phase Change Materials and the Quest for Metavalent Bonding. *Adv. Mater.* **30,** 1706735 (2018).

6. Lucovsky, G. & White, R. M. Effects of Resonance Bonding on the Properties of Crystalline and Amorphous Semiconductors. *Phys. Rev. B* **8,** 660–667 (1973).

7. Robertson, J., Xiong, K. & Peacock, P. W. Electronic and atomic structure of $Ge_2Sb_2Te_5$ phase change memory materials. *Thin Solid Films* **515,** 7538–7541 (2007).

8. Shportko, K. *et al.* Resonant bonding in crystalline phase-change materials. *Nat. Mater.* **7,** 653–658 (2008).

9. Dronskowski, R. *Computational Chemistry of Solid State Materials*. (Wiley-VCH, 2005).

10. Becke, A. D. & Edgecombe, K. E. A simple measure of electron localization in atomic and molecular systems. *J. Chem. Phys.* **92,** 5397 (1990).

11. Bader, R. F. W. *Atoms in Molecules: A Quantum Theory*. (Oxford University Press, 1994).

12. Silvi, B. & Savin, A. Classification of Chemical Bonds Based on Topological Analysis of Electron Localization Functions. *Nature* **371,** 683–686 (1994).

13. Gatti, C. Chemical bonding in crystals: New directions. *Z. Krist.* **220,** 399–457 (2005).

14. *Modern Charge Density Analysis*. (2012).

15. Silvi, B. & Gatti, C. Direct Space Representation of the Metallic Bond. *J. Phys. Chem. A* **104,** 947–953 (2000).

16. Feixas, F., Matito, E., Poater, J. & Solà, M. Quantifying aromaticity with electron delocalisation measures. *Chem. Soc. Rev.* **44,** 6434–6451 (2015).

17. Rahm, M. A Chemically Meaningful Measure of Electron Localization. *J. Chem. Theory Comput.* **11,** 3617–3628 (2015).

18. Baranov, A. I. & Kohout, M. Electron Localization and Delocalization Indices for Solids. *J. Comput. Chem.* **32,** 2064–2076 (2009).

19. Golub, P. & Baranov, A. I. Domain overlap matrices from plane-wave-based methods of electronic structure calculation. *J. Chem. Phys.* **145,** 154107 (2016).

20. Burdett, J. K. *Chemical Bonds: A Dialog*. (John Wiley \& Sons, 1997).

21. van Arkel, A. E. *Moleculen en kristallen*. (van Stockum, 1941).

22. Allen, L. C. Extension and Completion of the Periodic Table. *J. Am. Chem. Soc.* **114,** 1510–1511 (1992).

23. Jensen, W. B. A Quantitative van Arkel Diagram. *J. Chem. Educ.* **72,** 395 (1995).

24. Phillips, J. C. & van Vechten, J. A. Dielectric Classification of Crystal Structures, Ionization Potentials, and Band Structures. *Phys. Rev. Lett.* **22,** 705–708 (1969).

25. St. John, J. & Bloch, A. N. Quantum-Defect Electronegativity Scale for Nontransition Elements. *Phys. Rev. Lett.* **33,** 1095–1098 (1974).

26. Lencer, D. *et al.* A map for phase-change materials. *Nat. Mater.* **7,** 972–977 (2008).

27. Esser, M., Deringer, V. L., Wuttig, M. & Dronskowski, R. Orbital mixing in solids as a descriptor for materials mapping. *Solid State Commun.* **203,** 31–34 (2015).

28. Rahm, M. & Hoffmann, R. Distinguishing Bonds. *J. Am. Chem. Soc.* **138,** 3731–3744 (2016).

29. Mori-Sánchez, P., Martín Pendás, A. & Luaña, V. A classification of covalent, ionic, and metallic solids based on the electron density. *J. Am. Chem. Soc.* **124,** 14721–14723 (2002).

30. Grabowski, S. J. What Is the Covalency of Hydrogen Bonding? *Chem. Rev.* **111,** 2597–2625 (2011).

31. Wuttig, M. & Yamada, N. Phase-change materials for rewriteable data storage. *Nat. Mater.* **6,** 824–832 (2007).

32. Deringer, V. L., Dronskowski, R. & Wuttig, M. Microscopic Complexity in Phase-Change Materials and its Role for Applications. *Adv. Funct. Mater.* **25,** 6343–6359 (2015).

33. Lee, S. *et al.* Resonant bonding leads to low lattice thermal conductivity. *Nat. Commun.* **5,** 3525 (2014).

34. Cagnoni, M., Führen, D. & Wuttig, M. Thermoelectric Performance of IV–VI Compounds with Octahedral-Like Coordination: A Chemical-Bonding Perspective. *Adv. Mater.* **30,** 1801787 (2018).

35. Astakhov, A. A. & Tsirelson, V. G. Spatially resolved characterization of electron localization and delocalization in molecules: Extending the Kohn-Resta approach. *Int. J. Quantum Chem.* e25600 (2018). doi:10.1002/qua.25600

36. Raty, J.-Y. *et al.* Aging mechanisms in amorphous phase-change materials. *Nat. Commun.* **6,** 7467 (2015).

Acknowledgements

J.-Y.R. acknowledges computational resources provided by the CÉCI funded by the F.R.S.-FNRS under Grant No. 2.5020.11 and the Tier-1 supercomputer of the Fédération Wallonie-Bruxelles, infrastructure funded by the Walloon Region under grant agreement n°1117545. J.-Y.R acknowledges support from the Communaute française de Belgique through an ARC grant (AIMED 15/19-09). M.S. acknowledges computational resources provided by JARA-HPC (projects JARA0150, JARA0176, and JARA0183) and additional computing time provided by Prof. R. Mazzarello (Institute for Theoretical Solid State Physics, RWTH Aachen University). V.L.D. acknowledges a Leverhulme Early Career Fellowship and support from the Isaac Newton Trust. C.G. acknowledges partial support by the Danish National Research Foundation (Center for Materials Crystallography, DNRF93). This work was supported by Deutsche Forschungsgemeinschaft (DFG) through SFB 917 "Nanoswitches". Moreover, the research leading to these results has received funding from the European Union Seventh Framework Programme (FP7/2007-2013) under grant agreement no. 340698, as well as the Excellence Initiative (Distinguished Professorship).

Supplementary Materials

Methods

The optimised structures of all compounds were first studied the ABINIT Density Functional Theory code[37], using the PBE exchange-correlation functional[38] and projector augmented-wave (PAW) potentials[39–41]. Wavefunctions for relaxed structures were then used to determine Bader's basins and delocalization/localization indices (DIs/LIs) among/within such basins. Central to the evaluation of DIs and LIs is the calculation of the so-called Domain Overlap Matrices (DOM) over Bader's basins. This task is routinely performed for systems *in vacuo* described by localised basis sets, but only very recently has it been extended also to the realm of plane-wave based methods and periodic systems. In particular, we adopted the efficient algorithm for calculating the DOM elements implemented by Golub and Baranov for PAW method as a general purpose module of the program DGRID interfaced to the output of ABINIT code[19]. Bader's basins were obtained by a discrete-grid technique[42,43].

The DOM represent key ingredients for integration of the non-classical part of the electron pair density over atoms basins. Integration of such density over a single atomic basin Ω yields the localization index, $LI(\Omega)$, measuring the quantity of electrons which are fully localised in the atomic basin, in general almost all of the core electrons and, depending on the atom type and of its specific chemical environment, a small or larger fraction of the valence electrons. On the other hand, when the exchange-correlation density is integrated over a pair of atomic basins (denoted Ω_1 and Ω_2), one obtains the *delocalization index* $\delta(\Omega_1,\Omega_2)$, measuring the number of electron *pairs* being shared between the two atoms. Twice $\delta(\Omega_1,\Omega_2)$ therefore corresponds to the absolute number of electrons shared (ES), and this quantity forms the *y*-axis of the map in Fig. 1.

Integration of the non-classical exchange-(correlation) part of the electron pair density function satisfies the sum rule,

$$N(\Omega) = LI(\Omega) + \frac{1}{2}\sum_{\Omega' \neq \Omega} \delta(\Omega', \Omega), \qquad (1)$$

i.e., the sum of the localization and half of the delocalization indices of an atom Ω with all other basins Ω' equals the *electron population* of each atom Ω, $N(\Omega)$. The difference between the number of electrons of the bare atom (or, equivalently, of its nuclear charge) and the electron population $N(\Omega)$ yields

the atomic charge of Ω. For binary compounds and for those having only one unique crystallographic position per atom, this quantity may be denoted as "electrons transferred" (ET; the *x*-axis in Fig. 1).

DI values may slightly differ from what would be expected from classical bonding views. For instance, if silicon is taken as an example of a perfectly covalently bonded crystal, one would expect sharing of a full electron pair between each pair of first neighbours and no electron charge transferred, that is ES=2 (formal bond order of one) and ET=0, respectively. However, this would be the result one would obtain for a fictitious perfectly covalently bonded crystal in the absence of coulomb correlation treatment, like, rigorously, for the Hartree–Fock mono-determinantal approach and partly for the DFT Kohn-Sham approach. When such correlation is instead explicitly introduced, the effect of α, β correlation on bonding is that of decreasing the delocalization ability of opposite spin electrons, thereby leading to a general decrease of ES relative to the value that would be expected from the formal bond order. In real systems, electron pair sharing is often significantly below that anticipated from the formal bond order, as illustrated for Si, Ge, and Sn in Fig. 1, and the number of electrons entirely localised on the atom, LI(Ω), is consequently greater than the difference between its electron population and the ES value associated to the formal bond order multiplied by the number of bonds it forms (Eq. 1).

The data plotted in Fig. 2 (Z^*, ε_∞ and mode Grüneisen parameters) are partly taken from Ref. [4] and partly computed here. Note that Z* and ε_∞ values given here are averaged over atoms (absolute values) and directions, respectively. These data were obtained with the ABINIT code, using linear response and including LO–TO splitting for ionic systems[44]. Norm-conserving pseudopotentials of the Vanderbilt type[45] were used, including semicore states for elements such as Bi, Ge, Ga, In, Se and Sn, and spin–orbit coupling in the case of PbTe. Convergence on energies and forces upon plane-wave cutoff energies and *k*-point grid was tested, in particular regarding the absence of imaginary frequency phonons at Γ. The Born effective charges plotted are the average of the absolute values. The mode Grüneisen parameters are computed by varying the cell volume by 0.3% and relaxing the structure when needed.

For the out-of-equilibrium structures, such as the cubic GeTe phase, or phases with variable Peierls distortion, the cell was relaxed with imposed symmetry (cubic) or imposed Peierls distortion ratio (via the *R*3*m* fractional atomic position parameter).

Table S1: Materials computationally characterised in this work, as described in the Methods section above; numerical data for structural, bonding, and physical properties are listed here.

	Structure	Bonding mechanism	Electrons transferred	Electrons shared	Z^*	γ_{TO}	ε_∞
Elements:							
Al	$Fm\bar{3}m$	metallic	0	0.514	-	-	-
Ag	$Fm\bar{3}m$	metallic	0	0.486	-	-	-
Sn^{α}	$Fd\bar{3}m$	covalent	0	1.508	-	-	24.0
Pb	$Fm\bar{3}m$	metallic	0	0.452	-	-	-
Si	$Fd\bar{3}m$	covalent	0	1.680	-	1.0	13.0
Ge	$Fd\bar{3}m$	covalent	0	1.568	-	1.1	16.0
Na	$Im\bar{3}m$	metallic	0	0.200	-	-	-
Mg	$P6_3/mmc$	metallic	0	0.398	-	-	-
Ca*	$P6_3/mmc$	metallic	0	0.408	-	-	-
$C^{diamond}$	$Fd\bar{3}m$	covalent	0	1.826	-	-	5.8
$C^{graphite}$	$P6_3/mmc$	resonant	0	2.400	-	-	-

Table S1 (continued).

	Structure	Bonding mechanism	Electrons trans-ferred	Electrons shared	Z^*	γ_{TO}	ε_∞
Intermetallics:							
NiAl	$Pm\bar{3}m$	metallic	0.49	0.548	-	2.0	-
TiAl	$P4/mmm$	metallic	0.38	0.624	-	1.8	-
IIIA-VA compounds:							
AlN	$P6_3mc$	ionic	2.40	0.512	2.55	1.1	4.5
AlP	$F\bar{4}3m$	ionic	2.02	0.768	2.25	1.2	8.2
AlAs	$F\bar{4}3m$	ionic	1.91	0.836	2.15	1.1	9.8
AlSb	$F\bar{4}3m$	ionic	1.68	0.944	1.89	1.1	12.7
AlBi	$F\bar{4}3m$	ionic	1.59	0.992	1.87	1.5	22.2
GaN	$P6_3mc$	covalent	1.56	1.200	2.69	1.6	6.0
GaP	$F\bar{4}3m$	covalent	0.81	1.424	2.20	1.2	11.1
GaAs	$F\bar{4}3m$	covalent	0.68	1.400	2.20	1.2	14.5
GaSb	$F\bar{4}3m$	covalent	0.30	1.436	1.91	1.2	23.2
InN*	$F\bar{4}3m$	covalent	1.43	1.276	-	1.6	-
InP	$F\bar{4}3m$	covalent	0.88	1.416	2.60	1.3	12.7
InAs	$F\bar{4}3m$	covalent	0.72	1.400	2.74	1.3	16.3
InSb	$F\bar{4}3m$	covalent	0.55	1.388	2.50	1.4	21.3
IIA-VIA compounds:							
BeO	$P6_3mc$	ionic	1.73	0.278	1.80	1.7	3.1
BeS	$F\bar{4}3m$	ionic	1.60	0.386	1.61	1.6	5.3
BeSe	$F\bar{4}3m$	ionic	1.54	0.404	1.56	0.3	6.0
BeTe	$F\bar{4}3m$	ionic	1.45	0.508	1.34	1.8	7.4
MgO	$Fm\bar{3}m$	ionic	1.70	0.244	2.00	2.5	3.2
MgS	$Fm\bar{3}m$	ionic	1.67	0.236	2.35	3.1	5.4
MgSe*	$F\bar{4}3m$	ionic	1.59	0.408	1.91	1.5	4.7
MgTe	$F\bar{4}3m$	ionic	1.55	0.432	1.95	1.5	5.6
CaO	$Fm\bar{3}m$	ionic	1.48	0.468	2.35	3.0	3.8
CaS	$Fm\bar{3}m$	ionic	1.46	0.428	2.37	2.5	5.0
CaSe	$Fm\bar{3}m$	ionic	1.45	0.424	2.38	2.2	5.6
CaTe	$Fm\bar{3}m$	ionic	1.42	0.420	2.42	1.9	6.6
SrO	$Fm\bar{3}m$	ionic	1.48	0.500	2.43	3.3	3.8
SrS	$Fm\bar{3}m$	ionic	1.47	0.460	2.40	2.3	4.6
SrSe	$Fm\bar{3}m$	ionic	1.45	0.460	2.40	2.3	5.1
SrTe	$Fm\bar{3}m$	ionic	1.43	0.448	2.43	2.4	5.9
BaS	$Fm\bar{3}m$	ionic	1.43	0.536	2.60	2.6	4.8
BaSe	$Fm\bar{3}m$	ionic	1.39	0.536	2.59	2.5	5.3
BaTe	$Fm\bar{3}m$	ionic	1.37	0.538	2.59	2.4	5.9
IIB-VIA compounds:							
ZnO*	$F\bar{4}3m$	covalent	1.22	0.984	-	-	-
ZnS	$F\bar{4}3m$	covalent	0.88	1.168	2.00	1.8	5.8
ZnS$^{\text{Wurtzite}*}$	$P6_3mc$	covalent	0.91	1.116	-	-	-
ZnSe	$F\bar{4}3m$	covalent	0.67	1.172	2.09	1.8	7.3
ZnTe	$F\bar{4}3m$	covalent	0.43	1.232	2.08	1.8	9.0
CdS	$F\bar{4}3m$	covalent	0.85	1.156	2.24	1.9	6.4
CdSe	$F\bar{4}3m$	covalent	0.72	1.164	2.33	1.9	7.4
CdTe	$F\bar{4}3m$	covalent	0.52	1.220	2.33	1.9	8.9
HgS	$F\bar{4}3m$	covalent	0.55	1.336	3.15	3.3	24.6

Table S1 (continued).

	Structure	Bonding mechanism	Electrons trans-ferred	Electrons shared	Z^*	γ_{TO}	ε_∞
HgSe	$F\bar{4}3m$	covalent	0.40	1.324	3.38	2.6	19.9
HgTe	$F\bar{4}3m$	covalent	0.10	1.368	3.30	2.0	20.2
IA-VIIA compounds:							
NaCl	$Fm\bar{3}m$	ionic	0.87	0.140	1.10	2.4	2.5
NaF	$Fm\bar{3}m$	ionic	0.88	0.150	1.02	2.5	1.9
KF	$Fm\bar{3}m$	ionic	0.86	0.228	1.13	2.7	2.0
KCl	$Fm\bar{3}m$	ionic	0.84	0.208	1.16	2.8	2.3
KBr	$Fm\bar{3}m$	ionic	0.83	0.220	1.14	3.0	2.5
KI	$Fm\bar{3}m$	ionic	0.82	0.196	1.16	2.8	2.8
RbCl	$Fm\bar{3}m$	ionic	0.85	0.234	1.17	2.7	2.3
RbBr	$Fm\bar{3}m$	ionic	0.84	0.230	1.16	2.7	2.5
RbBr$^{Pm\bar{3}m*}$	$Pm\bar{3}m$	ionic	0.83	0.166	1.24	-	2.8
CsF	$Fm\bar{3}m$	ionic	0.88	0.274	1.30	3.6	2.3
CsF$^{Pm\bar{3}m*}$	$Pm\bar{3}m$	ionic	0.87	0.182	1.34	-	2.6
IVA-VIA compounds:							
GeSe	$Pnma$	covalent	0.65	1.376	2.96	1.4	16.7
GeTe^{220u*}	$R3m$, *dist.*	covalent	0.34	1.608	2.70	-	19.2
GeTe^{221u*}	$R3m$, *dist.*	covalent	0.33	1.572	2.97	-	21.6
GeTe^{224u*}	$R3m$, *dist.*	covalent	0.35	1.500	3.50	-	20.3
GeTe^{227u*}	$R3m$, *dist.*	covalent	0.34	1.444	3.95	-	29.2
GeTe^{ortho*}	$Pnma$	covalent	0.37	1.424	3.50	-	27.9
GeTe^{230u*}	$R3m$, *dist.*	covalent	0.36	1.384	4.43	-	32.3
GeTe^{233u*}	$R3m$, *dist.*	covalent	0.36	1.324	5.01	-	36.0
GeTe^{R3m}	$R3m$	metavalent	0.34	1.240	5.98	-	44.1
GeTe^{239u*}	$R3m$, *dist.*	metavalent	0.35	1.184	6.53	-	49.3
GeTe^{242u*}	$R3m$, *dist.*	metavalent	0.36	1.112	7.39	-	60.8
GeTe^{245u*}	$R3m$, *dist.*	metavalent	0.37	1.028	8.48	-	75.2
GeTe^{cub*}	$Fm\bar{3}m$	metavalent	0.35	0.900	9.42	-	91.5
SnO	$P4/nmm$	covalent	1.27	0.888	2.96	5.7	7.3
SnS	$Pnma$	covalent	0.97	1.120	3.39	1.3	14.1
SnSe	$Pnma$	covalent	0.83	1.244	3.49	2.0	17.1
SnTe	$Fm\bar{3}m$, *dist.*	metavalent	0.63	0.940	6.65	5.8	77.0
SnTe^{cub*}	$Fm\bar{3}m$	metavalent	0.63	0.848	-	-	-
PbO	$P4/nmm$	covalent	1.17	0.944	2.76	1.0	6.1
PbSe^{u2300*}	$Fm\bar{3}m$, *dist.*	covalent	0.85	1.144	3.65	-	15.0
PbSe^{u2400*}	$Fm\bar{3}m$, *dist.*	metavalent	0.87	0.968	4.42	-	18.4
PbSe^{u2440*}	$Fm\bar{3}m$, *dist.*	metavalent	0.87	0.884	4.68	-	19.6
PbSe^{u2464*}	$Fm\bar{3}m$, *dist.*	metavalent	0.87	0.840	4.72	-	20.2
PbSe^{u2482*}	$Fm\bar{3}m$, *dist.*	metavalent	0.875	0.804	4.75	-	20.5
PbSe	$Fm\bar{3}m$	metavalent	0.86	0.764	4.81	15.0	20.4
PbTe^{u2300*}	$Fm\bar{3}m$, *dist.*	covalent	0.64	1.232	3.87	-	19.4
PbTe^{u2400*}	$Fm\bar{3}m$, *dist.*	metavalent	0.67	1.040	4.96	-	23.2
PbTe^{u2440*}	$Fm\bar{3}m$, *dist.*	metavalent	0.68	0.948	5.44	-	25.4
PbTe^{u2464*}	$Fm\bar{3}m$, *dist.*	metavalent	0.685	0.888	5.61	-	26.2
PbTe^{u2482*}	$Fm\bar{3}m$, *dist.*	metavalent	0.68	0.848	5.70	-	26.6
PbTe	$Fm\bar{3}m$	metavalent	0.68	0.804	5.70	15.6	27.3

* indicates metastable phases; the label "dist." signifies gradual Peierls distortions (cf. Fig. 3).

Table S1 (continued).

	Structure	Bonding mechanism	Electrons trans-ferred	Electrons shared	Z^*	γ_{TO}	ε_∞
Ternary compounds:							
$AgBiSe_2$	$R\bar{3}m$	metavalent	0.64	0.860	3.97	6.6	24.3
$AgBiTe_2$	$R\bar{3}m$	metavalent	0.36	0.91	4.25	6.8	57.6
$AgSbTe_2$	$R\bar{3}m$	metavalent	0.28	0.934	4.30	3.0	39.2

Supplementary References

37. Gonze, X. *et al.* ABINIT: First-principles approach to material and nanosystem properties. *Comput. Phys. Commun.* **180,** 2582–2615 (2009).

38. Perdew, J. P., Burke, K. & Ernzerhof, M. Generalized Gradient Approximation Made Simple. *Phys. Rev. Lett.* **77,** 3865–3868 (1996).

39. Blöchl, P. E. Projector augmented-wave method. *Phys. Rev. B* **50,** 17953–17979 (1994).

40. Torrent, M., Jollet, F., Bottin, F., Zérah, G. & Gonze, X. Implementation of the projector augmented-wave method in the ABINIT code: Application to the study of iron under pressure. *Comput. Mater. Sci.* **42,** 337–351 (2008).

41. Jollet, F., Torrent, M. & Holzwarth, N. Generation of Projector Augmented-Wave atomic data: A 71 element validated table in the XML format. *Comput. Phys. Commun.* **185,** 1246–1254 (2014).

42. Baranov, A. I. & Kohout, M. Topological analysis of real space properties for the solid-state full-potential APW DFT method. *J. Phys. Chem. Solids* **71,** 1350–1356 (2010).

43. Kohout, M. DGrid-4.6, User Manual, Radebeul, 2016, available online at http://www.cpfs.mpg.de/~kohout/dgrid.html.

44. Gonze, X. & Lee, C. Dynamical matrices, Born effective charges, dielectric permittivity tensors, and interatomic force constants from density-functional perturbation theory. *Phys. Rev. B* **55,** 10355–10368 (1997).

45. Hamann, D. R. Optimized norm-conserving Vanderbilt pseudopotentials. *Phys. Rev. B* **88,** 085117 (2013).